INTERNATIONAL JOURNAL FOR NUMERICAL METHODS IN FLUIDS
*Int. J. Numer. Meth. Fluids* **28**: 293–315 (1998)

# A FRACTIONAL STEP METHOD FOR UNSTEADY FREE-SURFACE FLOW WITH APPLICATIONS TO NON-LINEAR WAVE DYNAMICS

STEFAN MAYER*, ANTOINE GARAPON AND LARS. S. SØRENSEN

*International Research Centre for Computational Hydrodynamics (ICCH), Agern Allé 5, DK-2970 Hørsholm, Denmark*

## SUMMARY

A fractional step method is developed for solving the time dependent two-dimensional Euler equations with full non-linear free-surface boundary conditions. The geometry of the free surface is described by a height function, and its evolution is tracked by integrating in time the kinematic boundary conditions based on the free-surface volume flux. The fluid domain is discretised by adapting a time-varying curvilinear grid to all boundaries, including the free surface. Mass and momentum equations are discretised by a conservative finite volume formulation, taking into account the time dependency of the grid. A fractional step type method is developed for integrating the fluid motion in time. The method is applied to a non-linear standing wave in a square container, testing for compliance with mass and energy conservation and comparing computed wave period with other results. Non-linear travelling waves are simulated in channels with either constant depth or varying depth and non-linear wave processes involving both triad interactions and quartet interactions are studied. Results are compared with both experimental data and theoretical results and excellent agreement is found. Interaction of waves and currents is studied. The blocking of waves in an opposing current is simulated and found to show good agreement with theoretical results. The method is intended to be a first step towards a full description of wave dynamics interacting with structures and currents. © 1998 John Wiley & Sons, Ltd.

KEY WORDS: Euler equations; free surface; gravity waves; finite volume method; fractional step method

## 1. INTRODUCTION

Numerical studies of free-surface flows involving gravity waves have typically been divided into two distinct approaches. Either the hypothesis of irrotational flow is chosen, leading to a potential flow formulation, which is often solved with boundary integral equation methods (BIEM) or spectral methods; or the Navier–Stokes or Euler equations are solved without further simplification. For references see the review by Floryan and Rasmussen [1] and Tsai and Yue [2].

In the potential flow approach, unsteady flow can be described accurately, e.g. unsteady gravity waves of finite amplitudes can be simulated with all non-linear effects and without any significant damping [3–6]. However, the interaction of waves with currents, and in particular with rotational velocity fields, is difficult to describe with these methods due to the inherent assumptions. Neither the effects of viscosity or turbulence on the wave motion can be described.

* Correspondence to: International Research Centre for Computational Hydrodynamics (ICCH), Agern Allé 5, DK-2970 Hørsholm, Denmark. Tel: +45 45769555, Fax: +45 45762567, E-mail: icch@dhi.dk

CCC 0271–2091/98/120293–23$17.50

*Received April 1997*
*Revised July 1997*

In principle, no such restrictions are imposed when solving the Navier–Stokes equations. However, not many computations of unsteady gravity waves have been reported in the literature [7–11]. Furthermore, it seems, that solutions to the unsteady Navier–Stokes or Euler equations, including a fully non-linear free-surface description, have usually suffered from relatively large numerical errors which did not allow accurate long term simulations of travelling gravity waves. The origin of the errors are believed to be found mainly in some of the following problems.

First of all, an accurate description of the free-surface geometry and its evolution in time is very difficult unless the fluid region is discretised exactly within its boundaries by using a surface-adaptive grid, which is opposite to the marker and cell (MAC) or volume of fluid (VOF) methods [7,9,12]. Then the transient governing equations must be formulated within a moving frame of reference. Such an approach has been introduced by e.g. Chan [8] and is often termed the arbitrary Lagrangian–Eulerian (ALE) method. However, the complexity of the algorithms is increased, time-accuracy is sacrificed and numerical damping is introduced by introducing time varying grids [1].

Secondly, in incompressible flow the governing equations are usually modified in order to ensure well-posed coupling between the velocity field and the pressure field. This is done either by the introduction of artificial compressibility or by using segregated methods such as the SIMPLE/PISO family, the MAC scheme or the fractional step approach. While an implementation of pressure boundary conditions in these methods is relatively easy for rigid boundaries, this is not the case along a free surface, because an accurate specification of the absolute value of the pressure is required in order to properly describe the transfer between potential and kinetic energy in the wave motion.

This study focuses on the applicability of Navier–Stokes and Euler codes for simulating travelling gravity waves in a numerical wave-tank, and an attempt is made to overcome some of the difficulties mentioned above. Hence, the aim of this study is to compute unsteady free-surface flow with an accuracy which is comparable with that achieved by conventional fully non-linear potential flow methods.

A finite volume code employing a cell-centred variable layout on general curvilinear grids is extended to moving grids and the flow is integrated in time by a modified fractional step method. The free surface is described by a height function and its evolution tracked by integrating in time a flux-based form of the kinematic free-surface boundary condition. The method is applied to simple two-dimensional geometries, mostly being wave tanks of different shapes. Usually, neither viscosity nor turbulence have a significant influence on the wave motion in wave tanks, therefore, the study is restricted to the Euler case. By doing so, the intricate problems of the intersection between the free surface with side walls can be simplified due to the imposed slip conditions along wall boundaries. Further, without the need of grid refinement in the boundary layer region, computational resources can be saved. Finally, the criterion of energy conservation can be applied rigorously in the inviscid case to evaluate numerical damping characteristics. However, the extension of the method to viscous flow is, in principle, straightforward and has been successfully tested.

The method is tested for various wave problems. Standing waves in closed containers are simulated, examining for compliance with mass and energy conservation laws and testing for dependency on both space and time discretisation. Non-linear travelling waves are simulated in a channel with either constant depth or varying depth, and non-linear wave processes involving both triad wave interactions and quartet wave interactions are studied. Finally, interaction of waves and currents is simulated, including wave blocking conditions.

 

## 2. MATHEMATICAL FORMULATION

The two-dimensional Euler equations may be written as

$$\nabla \cdot \boldsymbol{u} = 0, \tag{1}$$

$$\frac{\partial \boldsymbol{u}}{\partial t} + \boldsymbol{u} \cdot \nabla \boldsymbol{u} = -\nabla p, \tag{2}$$

where $\boldsymbol{u}$ is the fluid velocity vector, and $p$ denotes the dynamic excess pressure, being normalised with the fluid density. By excluding the mean hydrostatic pressure component from $p$, the gravitational source term in Equation (2) is avoided. The gravitational forcing then only appears in the dynamic free-surface boundary condition.

For description of the free-surface geometry, a co-ordinate system is defined by the unit-length basis vectors $\boldsymbol{e}_\mathrm{v}$ and $\boldsymbol{e}_\mathrm{h}$ in the vertical and horizontal direction, respectively. Assuming the free surface to be single valued in the direction of $\boldsymbol{e}_\mathrm{v}$, a local free-surface position vector may be expressed as

$$\boldsymbol{r} = \boldsymbol{r}_o + \eta \boldsymbol{e}_\mathrm{v}, \tag{3}$$

where the position vector $\boldsymbol{r}_o$ defines the equilibrium free-surface shape and $\eta$ denotes a local height variable.

The kinematic and dynamic boundary conditions are imposed along the free surface. The kinematic condition constraints fluid particles at the free surface to follow the local fluid velocity. In the variables, defined above, this may be expressed as

$$\frac{\partial \eta}{\partial t} = \boldsymbol{u} \cdot \boldsymbol{e}_\mathrm{v} - (\boldsymbol{u} \cdot \boldsymbol{e}_\mathrm{h}) \frac{\partial \eta}{\partial s}, \tag{4}$$

where $\partial/\partial s$ denotes the partial derivative in the direction of $\boldsymbol{e}_\mathrm{h}$. Since $\boldsymbol{r}_o$ satisfies $\partial/\partial s\ (\boldsymbol{r}_o \cdot \boldsymbol{e}_\mathrm{h}) = 0$, by definition, any local normal vector to the free surface satisfies

$$\boldsymbol{n} = (\boldsymbol{n} \cdot \boldsymbol{e}_\mathrm{v}) \left( \boldsymbol{e}_\mathrm{v} - \frac{\partial \eta}{\partial s} \boldsymbol{e}_\mathrm{h} \right). \tag{5}$$

Using Equation (5), the kinematic boundary condition, Equation (4), may be transformed to

$$\frac{\partial \eta}{\partial t} = \frac{\boldsymbol{u} \cdot \boldsymbol{n}}{\boldsymbol{n} \cdot \boldsymbol{e}_\mathrm{v}}. \tag{6}$$

Equation (6) expresses the temporal change of the free-surface geometry based on a local flux variable, since $\boldsymbol{u} \cdot \boldsymbol{n}$ denotes the volume flux through a segment of the free surface, being $|\boldsymbol{n}|$ wide.

The dynamic boundary condition expresses the equilibrium of stresses across the free surface. Since shear stresses are neglected, only a condition for the normal stress remains, yielding a Dirichlet boundary condition for the dynamic excess pressure

$$p = p_\mathrm{atm} - \boldsymbol{g} \cdot (\boldsymbol{r} - \boldsymbol{r}_0), \tag{7}$$

where $\boldsymbol{g}$ and $p_\mathrm{atm}$ denote the gravitational force vector and the atmospheric pressure in the air (normalised by fluid density), respectively. In the present work the atmospheric pressure is set to zero, $p_\mathrm{atm} = 0$.

At the remaining open boundaries, the normal velocity is specified to some value $U$

$$\boldsymbol{u} \cdot \boldsymbol{n} = U. \tag{8}$$

 

Slip conditions are imposed along wall boundaries

$$\boldsymbol{u} \cdot \boldsymbol{n} = 0. \tag{9}$$

## 3. NUMERICAL METHOD

The fluid domain is discretised by a curvilinear grid adapted to all fluid boundaries. All field variables are defined at cell centres, and the spatial discretisation follows the usual finite volume approach, where the governing equations are written as integral transport equations expressing the balance of fluxes for each cell. So the temporal change of a scalar field $\phi$ inside a cell is written as

$$\frac{\mathrm{d}}{\mathrm{d}t} \int_{\mathrm{cell}} \phi \, \mathrm{d}V = \int_{\mathrm{face}} F \, \mathrm{d}S, \tag{10}$$

where $F$ denote fluxes of $\phi$ across the cell boundary.

*Grid generation*. The free surface is discretised by a number of points $\boldsymbol{r}_i$, each corresponding to a cell face of the surface adapted grid. Cell vertex points along the surface are interpolated between these points by cubic B-splines.

The remaining boundaries are discretised by employing different stretching functions. Generally, an exponential stretching is employed in the vertical direction, concentrating horizontal grid lines near the free surface. The stretching is parameterised by the ratio between the increments at either end along a vertical grid line, $\alpha = \Delta y_{\mathrm{lower}}/\Delta y_{\mathrm{upper}}$.

Given the boundary vertex points, the interior vertex points of the grid are computed by transfinite interpolation with appropriate blending functions, as described by Thomson *et al.* [13]. Every four vertex points, indexed as $\xi_{i\pm1/2,j\pm1/2}$, define a computational cell with index $(i, j)$ (see Figure 1(a)). All variables are defined at cell centres, and in principle the spatial discretisation follows the usual finite volume approach for the cell centred variable layout.

### 3.1. Spatial discretisation

Field values are discretised to be constant within each cell and so fluxes are constant over faces, hence Equation (10) is discretised for each cell as

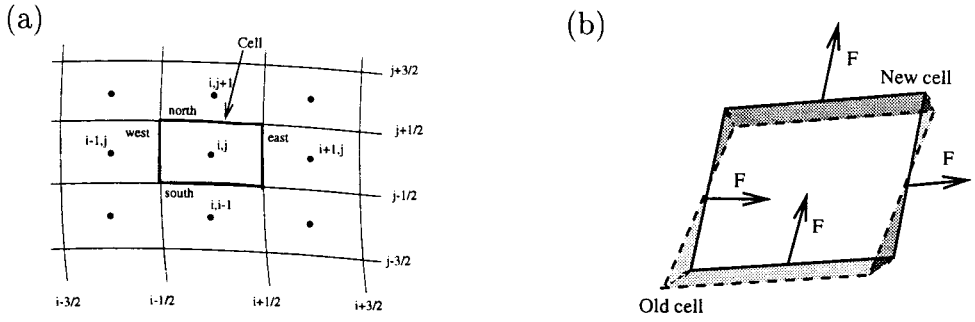


Figure 1. (a) Schematic drawing of finite volume cell and variable layout. (b) Geometrical representation of grid flux, light shaded and dark shaded areas representing positive contributions (out-flowing) and negative contributions (in-flowing), respectively.

 

$$\frac{\mathrm{d}}{\mathrm{d}t}(v\phi) = Df(\phi), \tag{11}$$

where $v$ denotes the cell volume and is found directly by geometrical considerations, while $f(\phi)$ denotes the integrated flux of $\phi$ over each face. The operator $D$ computes the signed sum of face values around a cell

$$D(f)_{i,j} = f_{i,j,\mathrm{e}} - f_{i,j,\mathrm{w}} + f_{i,j,\mathrm{n}} - f_{i,j,\mathrm{s}}, \tag{12}$$

where face values are indicated by the subscripts w, e, s, n, using the usual notation of 'west', 'east', 'south', 'north' cell faces, respectively.

At each face, the flux $f$ is divided into a convective, a diffusive and a grid-velocity part, the latter being close to the approach of Rosenfeld *et al.* [14],

$$f(\phi) = f_{\mathrm{conv}}(\phi) + f_{\mathrm{diff}}(\phi) + f_{\mathrm{grid}}(\phi), \tag{13}$$

where

$$f_{\mathrm{conv}}(\phi) = Q(\phi)I(\boldsymbol{u})\cdot\boldsymbol{n}, \tag{14}$$

$$f_{\mathrm{diff}}(\phi) = \kappa\boldsymbol{G}(\phi)\cdot\boldsymbol{n}, \tag{15}$$

$$f_{\mathrm{grid}}(\phi) = I(\phi)f_{\mathrm{g}}, \tag{16}$$

where $\boldsymbol{n}$ denotes the face normal vector, with $|\boldsymbol{n}|$ being the face area, $\kappa$ denotes a diffusivity and $f_{\mathrm{g}}$ is the grid flux, describing the motion of grid faces. $I$, $Q$ and $\boldsymbol{G}$ denote discretisation operators. The operator $I$ interpolates face values as the mean value of adjacent cell centre values to their common face, (e.g. east face of cell $(i, j)$),

$$I(\phi)_{i,j,\mathrm{e}} = \frac{1}{2}(\phi_{i,j} + \phi_{i+1,j}). \tag{17}$$

The operator $Q$ interpolates face values for the convective fluxes employing the QUICK upwind scheme (e.g. east face of cell $(i, j)$ and flow directed from west to east)

$$Q(\phi)_{i,j,\mathrm{e}} = \frac{1}{2}(\phi_{i,j} + \phi_{i+1,j}) - \frac{1}{8}(\phi_{i-1,j} - 2\phi_{i,j} + \phi_{i+1,j}). \tag{18}$$

The operator $\boldsymbol{G}$ evaluates the gradient of a field at the cell face, including cross derivative terms,

$$\boldsymbol{G}(\phi)_{i,j,\mathrm{e}} = \frac{\boldsymbol{n}_{i,j,\mathrm{e}}}{1/2\,(v_{i,j} + v_{i+1,j})}(\phi_{i+1,j} - \phi_{i,j}) + \frac{1/4\,(\boldsymbol{n}_{i,j,\mathrm{s}} + \boldsymbol{n}_{i,j,\mathrm{n}} + \boldsymbol{n}_{i+1,j,\mathrm{s}} + \boldsymbol{n}_{i+1,j,\mathrm{n}})}{1/2\,(v_{i,j} + v_{i+1,j})} \times \frac{1}{4}(\phi_{i,j+1} - \phi_{i,j-1} + \phi_{i+1,j+1} - \phi_{i+1,j-1}),$$

since $\boldsymbol{n}/v$ are contravariant basis vectors of the grid.

*3.1.1. Boundary conditions.* All boundary conditions are imposed implicitly at cell faces. They are implemented in the general form

$$a\phi + b\frac{\partial\phi}{\partial n} = r, \tag{19}$$

including both Neumann and Dirichlet conditions, specified by $a = 0$ and $b = 0$, respectively. Assuming the value $\phi_{\mathrm{b}}$ at the boundary face is implicitly known, the operators $I$ and $Q$ at boundary cell faces are given by

 

$$I_{\mathrm{b}}(\phi) = Q_{\mathrm{b}}(\phi) = \phi_{\mathrm{b}}. \tag{20}$$

The gradient operator $G$ at boundary cell faces is based on second-order one-sided differences, including cross-derivative terms (e.g. east boundary face)

$$\begin{aligned}
&\boldsymbol{G}_{\mathrm{b}}(\phi)_{i,j,\mathrm{e}} \\
&= \frac{\boldsymbol{n}_{i,j,\mathrm{e}}}{3/2\, v_{i,j} - 1/2\, v_{i-1,j}} \left( \frac{8}{3}\phi_{\mathrm{b}} - \frac{9}{3}\phi_{i,j} + \frac{1}{3}\phi_{i-1,j} \right) \\
&\quad + \frac{3/4\,(\boldsymbol{n}_{i,j,\mathrm{s}} + \boldsymbol{n}_{i,j,\mathrm{n}}) - 1/4\,(\boldsymbol{n}_{i+1,j,\mathrm{s}} + \boldsymbol{n}_{i+1,j,\mathrm{n}})}{3/2\, v_{i,j} - 1/2\, v_{i-1,j}} \left( \frac{3}{4}(\phi_{i,j+1} - \phi_{i,j-1}) \right. \\
&\quad \left. - \frac{1}{4}(\phi_{i-1,j+1} - \phi_{i-1,j-1}) \right).
\end{aligned} \tag{21}$$

The gradient in Equation (19) is approximated by use of Equation (21),

$$a\phi_{\mathrm{b}} + b\boldsymbol{G}_{\mathrm{b}}(\phi) \cdot \frac{\boldsymbol{n}}{|\boldsymbol{n}|} = r, \tag{22}$$

which can be solved for $\phi_{\mathrm{b}}$ and can be included implicitly through the use of $I_{\mathrm{b}}$, $Q_{\mathrm{b}}$ and $\boldsymbol{G}_{\mathrm{b}}$ in the spatial discretisation.

*3.1.2. Extrapolation of velocity at free surface*. In contrast to the general viscous case, in the Euler case the dynamic boundary condition is a pure pressure boundary condition because viscous stresses are not defined. Therefore, no boundary condition for the velocity field is imposed along the free surface. However, because the velocity is only defined at cell centres, but is needed at free-surface cell faces for the evaluation of fluxes, extrapolation of face values is required. In the present work, the velocity is extrapolated by use of the operator $I_{\mathrm{b}}$, according to Equations (20) and (22), as if homogeneous Neumann conditions were imposed,

$$\frac{\partial \boldsymbol{u}}{\partial n} = 0. \tag{23}$$

This procedure corresponds to first-order extrapolation.

### *3.2. Time discretisation*

*3.2.1. Overall procedure*. The overall procedure for integrating the system of fluid motion and free surface from time step $t^n$ to $t^{n+1}$ may be summarised as follows.

- A spatially discretised kinematic boundary condition is explicitly integrated in time, yielding the new free-surface geometry at time $t^{n+1}$.
- A new grid for $t^{n+1}$ is generated and grid fluxes are computed.
- The fluid velocity is integrated in time by a fractional step method.
- The pressure is obtained by solving the momentum equation on the basis of the new velocity field.

The entire time integration procedure is implemented for variable time steps. However, the time step is set to be constant below, for simplicity of documentation.

 

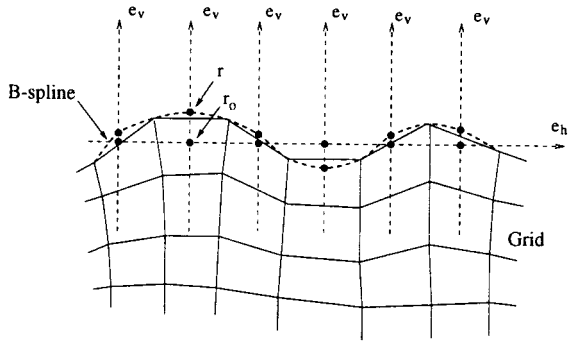


Figure 2. Description of the free-surface geometry by height function points moving along given direction $\boldsymbol{e}_v$. Interpolation of grid vertex points by cubic B-splines.

*3.2.2. Free surface*. In the present formulation, the surface height variable $\eta$ is discretised at centre points of free-surface cell faces. The flux-based form of the kinematic equation, Equation (6), is integrated over every free-surface cell face, yielding

$$\frac{\partial \eta}{\partial t} = \frac{f}{\boldsymbol{n} \cdot \boldsymbol{e}_v}, \tag{24}$$

where $\boldsymbol{n}$ is the face normal vector and $f = \boldsymbol{u} \cdot \boldsymbol{n}$ denotes the volume flux through the free-surface cell face. Equation (24) is numerically integrated from time step $n$ to $n+1$ by an explicit third-order Adams–Moulton multistep method, as

$$\eta^{n+1} = \eta^n + \Delta t \sum_{i=0}^{2} \alpha_i \frac{f^{n-i}}{\boldsymbol{n}^{n-i} \cdot \boldsymbol{e}_v}, \tag{25}$$

with

$$\alpha_0 = \frac{23}{12}, \qquad \alpha_1 = -\frac{16}{12}, \qquad \alpha_2 = \frac{5}{12}. \tag{26}$$

The flux variable and boundary conditions are defined at cell faces, but the free-surface geometry must be specified at cell vertex points when used for grid generation. Therefore, interpolation is required at some stage in the implementation of the kinematic boundary conditions (see Figure 2). In the present formulation, grid vertex points for time step $n+1$ are interpolated on the basis of the free-surface position vectors $\boldsymbol{r}^{n+1} = \boldsymbol{r}_o + \eta^{n+1}\boldsymbol{e}$ by employing cubic B-splines, in order to minimise the dissipation associated with interpolation. By basing the free-surface evolution on the local volume flux, global mass conservation can be ensured very accurately—the temporal volume change of the fluid domain reflecting accurately the global net flux through outer boundaries.

*3.2.3. Fluid domain*. The time integration of the velocity field is carried out by a second-order fractional step method, being close to that of Zang *et al.* [15]. However, it is extended to moving grids by an approach similar to that of Rosenfeld *et al.* [14]. Assume that solutions for velocity and pressure are known up to time step $t^n$, and grid and boundary conditions have been set for $t^{n+1}$. The velocity field at time $t^{n+1}$ is split into a predictor velocity field $\boldsymbol{u}^*$ and an irrotational correction $\nabla\phi$,

$$\boldsymbol{u}^{n+1} = \boldsymbol{u}^* + \nabla\phi. \tag{27}$$

 

Using an explicit Adams–Bashforth type scheme for the convective term and the pressure forcing, the momentum equations (2) are satisfied by $\boldsymbol{u}^*$ to second-order in time,

$$\frac{\boldsymbol{u}^* - \boldsymbol{u}^n}{\Delta t} = \left(\frac{3}{2}\nabla p^n - \frac{1}{2}\nabla p^{n-1}\right) - \left(\frac{3}{2}(\boldsymbol{u}\cdot\nabla\boldsymbol{u})^n - \frac{1}{2}(\boldsymbol{u}\cdot\nabla\boldsymbol{u})^{n-1}\right). \tag{28}$$

The correction $\nabla\phi$ is determined by restricting $\boldsymbol{u}^{n+1}$ to satisfy the continuity equation (1), hence

$$\nabla^2\phi = -\nabla\cdot\boldsymbol{u}^*. \tag{29}$$

In usual fractional step methods, the pressure forcing is evaluated in the predictor step at time $t^{n-1/2} = p^{n-1/2}\Delta t$ and is updated in time by the incrementation procedure,

$$p^{n+1/2} = p^{n-1/2} - \frac{1}{\Delta t}\phi. \tag{30}$$

The incrementation, Equation (30), is not trivial to perform on a moving grid system because the different fields $p^{n+1/2}$, $p^{n-1/2}$ and $\phi$ are defined on different grids (and grids at time step $t + 1/2(\Delta t)$ do not exist). Furthermore, the absolute value of the pressure field has to comply accurately to the dynamic free-surface condition. Although attempts have been made to derive algorithms of the form of Equation (30) with special consideration of the inhomogeneous Dirichlet boundary conditions for $\phi$ at the free surface, we did not succeed in controlling the transfer between kinetic energy in the flow and potential energy in the free-surface deformation to sufficient accuracy.

Instead of using the pressure updating procedure of the type in Equation (30), the pressure is evaluated at time $t^{n+1}$ by taking the divergence of the momentum equation (2),

$$\nabla^2 p = -\nabla\cdot(\boldsymbol{u}\cdot\nabla\boldsymbol{u}), \tag{31}$$

yielding a Poisson equation for the pressure field. As the boundary condition along the free surface, Equation (7) is imposed at every free-surface cell face,

$$p^{n+1} = -\boldsymbol{g}\cdot(\boldsymbol{r}^{n+1} - \boldsymbol{r}_0). \tag{32}$$

By projecting the momentum equation (2) onto the normal direction of the boundary, a Neumann boundary condition for the pressure is derived at the remaining boundaries,

$$\nabla p\cdot\boldsymbol{n} = -(\boldsymbol{u}\cdot\nabla\boldsymbol{u})\cdot\boldsymbol{n}. \tag{33}$$

The grid is moving as it adapts to the moving free surface, therefore, the discrete differential operators are time dependent with the grid. Furthermore, since all variables are stored as cell values, face values for evaluation of fluxes must be interpolated. This adds complexity to the resulting algorithm, compared with the general outline above. Using the above operator notation, the velocity time integration procedure may be expressed as follows.

$$\boldsymbol{u}^* v^{n+1} = \boldsymbol{u}^n v^n + \Delta t D\left[-\left(\frac{3}{2}(p\boldsymbol{n})^n - \frac{1}{2}(p\boldsymbol{n})^{n-1}\right) - \left(\frac{3}{2}(Q(\boldsymbol{u})f)^n - \frac{1}{2}(Q(\boldsymbol{u})f)^{n-1} + I\left(\frac{1}{2}(\boldsymbol{u}^n + \boldsymbol{u}^*)\right)\right) f_g^{n+1/2}\right], \tag{34}$$

$$f^* = I(\boldsymbol{u}^*)\cdot\boldsymbol{n}^{n+1}, \tag{35}$$

$$D(\boldsymbol{G}(\phi)\cdot\boldsymbol{n})^{n+1} = -D(f^*), \tag{36}$$

 

$$\boldsymbol{u}^{n+1} = \boldsymbol{u}^* + \frac{1}{v^{n+1}} D(I(\phi)\boldsymbol{n}^{n+1}), \tag{37}$$

$$f^{n+1} = f^* + (\boldsymbol{G}(\phi)\cdot\boldsymbol{n})^{n+1}. \tag{38}$$

While $f^*$ denotes the predictor flux field, and is not numerically divergence-free, $f^{n+1}$ is ensured to be divergence-free in the definition $D(f^{n+1}) = 0$, by means of step Equations (36) and (38). The grid flux terms are discretised in time with a trapezoidal scheme, since this semi-implicit treatment has been shown to be advantageous for both accuracy and stability. In terms of the present finite volume approach, $f_g^{n+1/2}$ is based on the area over which a given cell face is sweeping from time $t^n$ to $t^{n+1}$ (see Figure 1(b)). The geometrical evaluation of cell volumes $v$ and grid fluxes $f_g$, respectively, ensures that

$$v^{n+1} - v^n = -\Delta t D(f_g^{n+1/2}) \tag{39}$$

is exactly satisfied, which retains the conservative properties of the algorithm. Physically, Equation (39) implies that fluid moving with constant speed is not experiencing any erroneous acceleration due to the grid motion.

At the end of a time step the Poisson equation for the pressure, Equation (31), is discretised in space and solved,

$$D(\boldsymbol{G}(p)\cdot\boldsymbol{n})^{n+1} = -D\left(I\left(\frac{D(Q(\boldsymbol{u})f)}{v}\right)\cdot\boldsymbol{n}\right)^{n+1}. \tag{40}$$

*3.2.4. Solution of algebraic equations*. The implicit part of both the discretised momentum equation (34) and the Poisson equations (36) and (40) is written with nine-point stencils in a cell-by-cell form. While the discretised momentum equation (34) is solved iteratively by either point- or line-relaxation, the Poisson equations (36) and (40) are solved by a multigrid method, using standard coarsening and V-cycle relaxation. On every multigrid level either point-relaxation, line-relaxation, or an ILLU smoother is employed, depending on the grid.

*3.2.5. Wave generation*. For the generation of waves with angular frequency $\omega$ and phase $\phi$, a time varying velocity profile is imposed at one end of the fluid domain, being of the form

$$u_x = f_r[U_1(y)\sin(\varphi) + U_2(y)\sin(2\varphi)], \quad \varphi = \omega t + \theta, \tag{41}$$

allowing the control of both the primary wave and its second harmonic. The imposed velocity profiles $U_1(y)$, $U_2(y)$ may be either linear or rectangular as it might be physically imposed by flap- or piston-wave makers, see e.g. Reference [16], or Stokes velocity profiles may be imposed. Generally, the amplitude of the boundary velocity is superposed by a smoothly increasing 'ramp-function' $f_r(t)$ in order to prevent initial waves with amplitudes which are too high

$$f_r(t) = \begin{cases} \dfrac{t}{T} - \dfrac{1}{\pi}\sin\left(\pi\dfrac{t}{T}\right) & \text{for } 0 < t < T \\ 1 & \text{for } t > T \end{cases}, \tag{42}$$

where $T$ denotes the wave period.

 

*3.2.6. Wave absorption*. At the opposite end to the wave generator a numerical sponge layer is introduced within a region sizing two or more wave lengths (e.g. from $x_{\text{start}}$ to $x_{\text{end}}$, $|x_{\text{end}} - x_{\text{start}}| > 2L$). Both the elevation variable $\eta$ and the fluid velocity $\boldsymbol{u}$ at every time step are relaxed towards prescribed values, $\eta_p$ and $\boldsymbol{u}_p$, respectively, by a procedure of the form

$$\eta = (1-\gamma)\eta + \gamma\eta_p, \qquad \boldsymbol{u} = (1-\gamma)\boldsymbol{u} + \gamma\boldsymbol{u}_p, \tag{43}$$

where $\gamma$ denotes a relaxation parameter which increases very softly as the waves are entering at $x_{\text{start}}$ in order to prevent reflections. Throughout this work the variation of $\gamma$ has the form

$$\gamma(x) = b\beta^3 + (1-b)\beta^6, \qquad \beta = \frac{|x - x_{\text{start}}|}{|x_{\text{end}} - x_{\text{start}}|}. \tag{44}$$

The parameter $b$ determines the growth rate of the relaxation and is adjusted for the particular set-up.

## 4. RESULTS

### *4.1. Standing waves*

Standing Stokes waves have been extensively studied in the past and they are often known in a Fourier form. A description of a standing wave with steepness $ka = 0.1403$ was used, that includes the first eight harmonic components (e.g. to eighth-order in wave steepness $ka$), found by Agnon and Glozman [17]. Agnon and Glozman used an accurate Hamiltonian formulation and showed that the wave is exactly periodic over thousands of periods. Due to amplitude dispersion, the period was found to be $T_e = 1.00253 \times T_l$, $T_l = 2\pi/\sqrt{kg}$ being the period of the corresponding linear deep-water Stokes wave, with $k$ being the wave number.

At $t = 0$, in a square container with side length $L$ (being the wavelength), the free-surface elevation is prescribed, including the first eight harmonic components according to Agnon and Glozman [17], and fluid velocity is initially set to zero. Grids are generated with $N \times M$ cells,

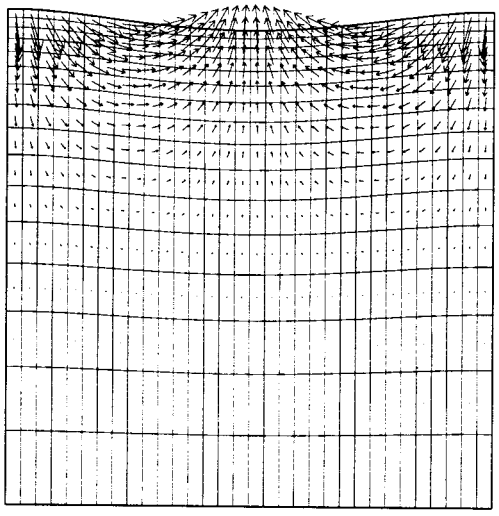

Figure 3. Standing wave of steepness $ka = 0.1403$. Fluid domain discretised by $32 \times 16$ cells, with equidistant horizontal resolution and stretched vertical discretisation ($\alpha = 10$). Velocity vectors are shown at cell centres.

 

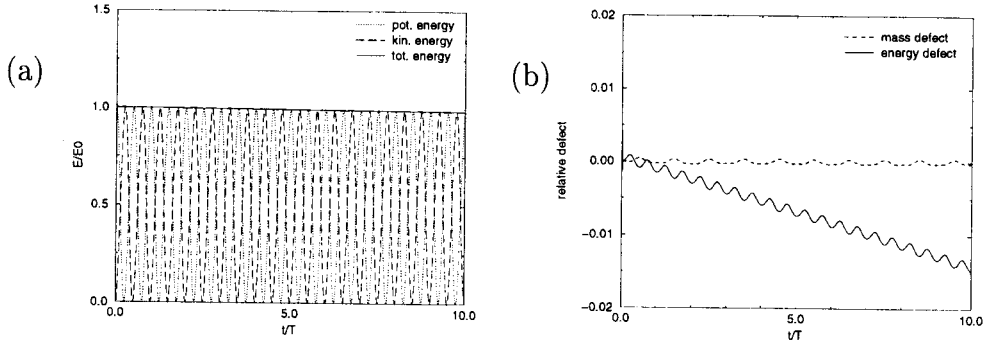


Figure 4. Standing wave of steepness $ka = 0.1403$ discretised in space by $64 \times 32$ cells and in time with time step $\Delta t/T_l = 0.009$. (a) Energy history; (b) relative volume defect $(V_{\text{tot}}(t) - V_{\text{tot}}(0))/(LH)$ and relative energy defect $(E_{\text{tot}}(t) - E_{\text{tot}}(0))/E_0$ as a function of time.

$N = 2M$ being equidistant horizontally and employing vertical stretching ($\alpha = 10$) (see Figure 3).

While the fluid and surface motion is computed in time, the total fluid volume $V_{\text{tot}}$, the kinetic energy $E_{\text{kin}}$, the potential energy $E_{\text{pot}}$ and the total energy $E_{\text{tot}} = E_{\text{kin}} + E_{\text{pot}}$ are evaluated (see Figure 4). The relative global volume defect $(V_{\text{tot}}(t) - V_{\text{tot}}(0))/(HL)$ is seen to

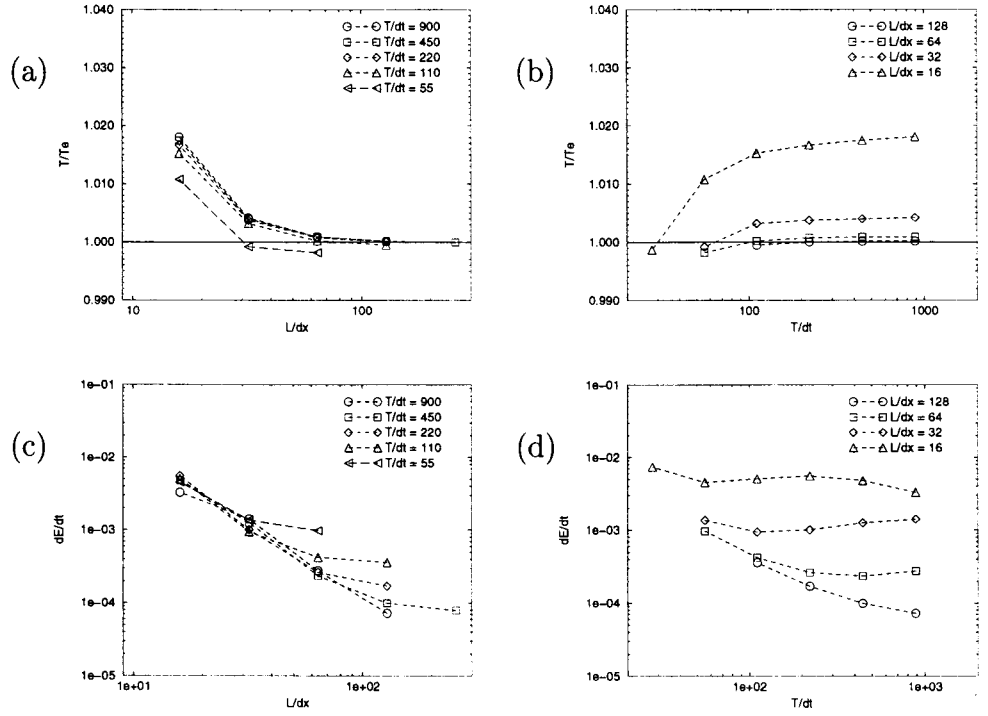


Figure 5. Standing wave of steepness $ka = 0.1403$. (a,b) Computed normalised wave period $T/T_e$ as function of space and time discretisation, respectively, $T_e = 1.00253(2\pi/\sqrt{kg})$ is the solution of Agnon and Glozman [1]. (c,d) Long term energy loss $(\mathrm{d}E_{\text{tot}}/\mathrm{d}t)/E|_0$ as a function of space and time discretisation, respectively. Ratio of grid points in vertical direction compared with horizontal direction is 1:2, the vertical discretisation using a stretching function is shown in Figure 3.

 

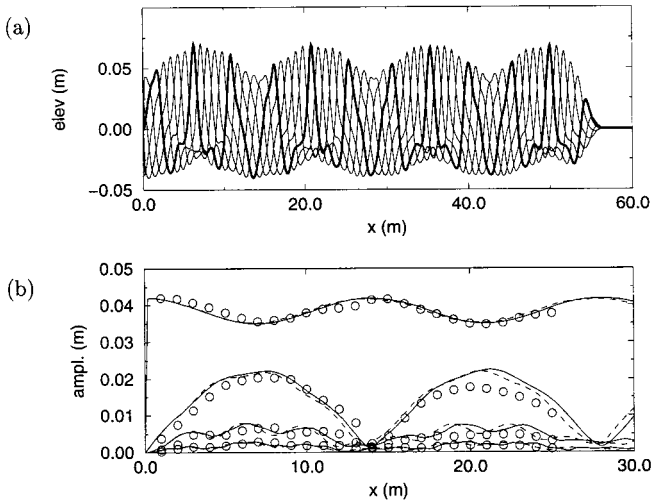


Figure 6. Propagation of waves generated by first-order piston wave maker. Depth $h = 0.4$ m, wave period $T = 2.5$ s and wave height $H = 0.084$ m. (a) Computed elevation profile at five phases during one period using discretisation $\Delta x = 0.03$ m, $\Delta t = 0.01$ s; (b) amplitudes of first four harmonic components. (—), computed, $\Delta x = 0.03$ m, $\Delta t = 0.01$ s; (-----), computed, $\Delta x = 0.06$ m, $\Delta t = 0.02$ s; (○), measured by Chapalain *et al.* [18].

oscillate with the wave period, the oscillations being due to the interpolation of grid vertex points from face centre points along the free surface. However, the variations appear to be reversible and the long term global volume defect is found to be negligible in all cases. The time history of the energy defect $(E_{\text{tot}}(t) - E_{\text{tot}}(0))/E_{\text{tot}}(0)$ is also superposed by variations within a wave period, however, it is clearly decreasing in average. While the oscillations are ascribed to errors in the integration of the energy over the fluid domain and are of minor importance, the results clearly show an average dissipative behaviour.

Both wave period and the energy loss are computed for different space and time discretisations (see Figure 5). While the computed wave period and the energy loss seem to converge with second-order in space discretisation given a constant time discretisation, the dependency on time discretisation is more complex. Given the space discretisation, the dissipation rate reaches a minimum at a given finite time step, and further refinement of the temporal discretisation causes the dissipation rate to increase. The convergence of the computed period, while second-order for moderate time steps, is slowed down for very small time steps.

### *4.2. Travelling waves*

*4.2.1. Triad interactions on horizontal bottom.* One of the simplest examples of triad interactions occurs when first-order monochromatic velocity boundary conditions are applied in shallow water. This will generate spurious free higher harmonics, in addition to bound higher-order waves, which are phase locked to the primary wave. The results will then be a spatial variation of wave profiles and statistics. A particular example is simulated here, which has been both experimentally and numerically investigated by Chapalain *et al.* [18] (Test A) and numerically by Madsen and Sørensen [19].

A rectangular velocity profile with a sinusoidal time variation (period $T = 2.5$ s) is imposed during 200 s, generating waves of height $H = 0.084$ m in a channel of depth $h = 0.4$ m and length $L_{\text{channel}} = 60$ m. The channel is discretised with $1024 \times 16$ and $2048 \times 32$ cells, and time steps of $\Delta t = 0.02$ and 0.01 s, respectively, are used. While the horizontal discretisation is

 

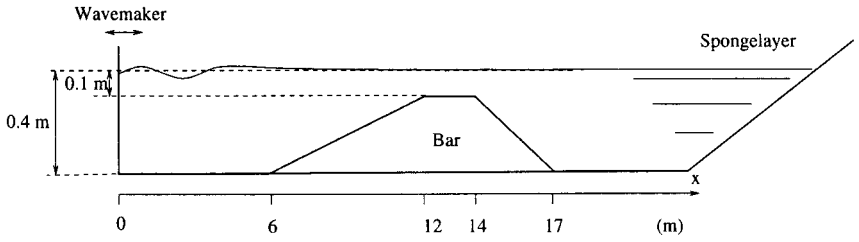


Figure 7. Wave tank with submerged bar on horizontal bottom.

equidistant, $\Delta x = 0.06$ and 0.03 m respectively, the vertical resolution is refined towards the free surface ($\alpha = 10$). Elevation profiles are shown in Figure 6(a), while the amplitudes of the first to fourth harmonics are shown as they vary along the channel in Figure 6(b). Both the beat length in the interaction between the harmonic components and the amplitudes of the higher harmonics are seen to be quite invariant with discretisation and to be in good agreement with the experimental data of Chapalain *et al.* [18].

*4.2.2. Shoaling wave over submerged bar*. The code is used for simulating the propagation of regular incident waves with period $T = 2.02$ s and height $H = 0.02$ m over a submerged bar on a horizontal bottom (see Figure 7). This test has been investigated both experimentally [20,21] and numerically [22–24] by numerous authors. On the upward slope the incoming wave is shoaling, with non-linearity generating bound higher harmonics, which travel phase-locked to the primary wave. On the downward slope these harmonics are released as free waves, resulting in an irregular wave pattern. The numerical reproduction of this pattern has shown to be very demanding with respect to the accuracy of the computed linear dispersion.

The problem is solved with different equidistant spatial discretisation in the horizontal direction ($\Delta x \approx \{0.015, 0.03, 0.06\}$ m), stretched vertical discretisation ($\alpha = 10$) and different

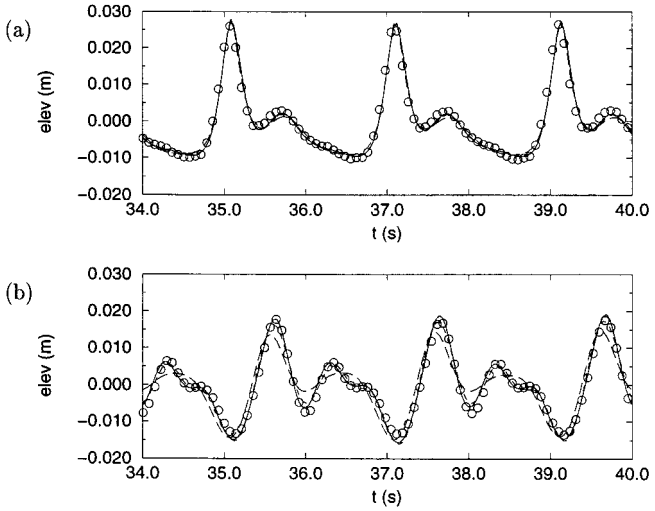


Figure 8. Propagation of regular waves with period $T = 2.02$ s and initial height $H = 0.02$ m over a submerged bar (see Figure 7). Time series of surface elevations at (a) a location on top of the bar, $x = 13.5$ m, and (b) behind the bar, $x = 21$ m. (○), measured by Luth *et al.* [21]; (—), computed, $\Delta x = 0.015$ m, $\Delta t = 0.01$ s; (-----), computed, $\Delta x = 0.03$ m, $\Delta t = 0.02$ s; (– – –), computed, $\Delta x = 0.06$ m, $\Delta t = 0.04$ s.

 

time steps ($\Delta t = \{0.01, 0.02, 0.04\}$ s). Waves are generated for 80 s in fluid initially at rest. Both the computed elevation and its Fourier transform are compared with measured data at selected locations (see Figures 8 and 9). The shoaling process on the upward slope of the bar is well described, even with the coarsest discretisation used. However, on the lee side of the bar, the spatial discretisation needs to be sufficiently fine to resolve the released higher harmonic waves, which are otherwise damped by numerical dissipation.

*4.2.3. Sideband instability of non-linear deep-water waves.* In their theoretical and experimental work, Benjamin and Feir [25] showed that weakly non-linear deep-water wave trains are unstable to modulational perturbations. Modulations by side band wave components gain energy by quartet interactions as the waves travel and the shape of the initial wave group evolves into massive wave pulses. Physically, these pulses are damped by wave breaking or evolve back into a wave group of almost the initial shape, hence the system shows recurrence. According to the stability analysis of Benjamin and Feir, the waves are most unstable to pertubational waves with the frequency shift $\delta = \pm ka$, where $ka$ is the steepness of the

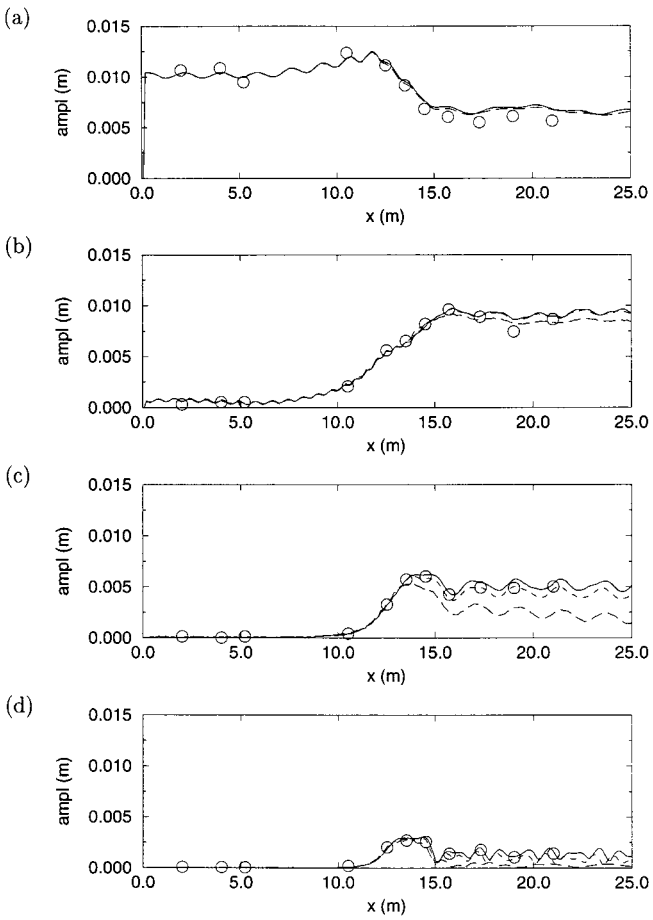


Figure 9. Propagation of regular waves with period $T = 2.02$ s and initial height $H = 0.02$ m over a submerged bar (see Figure 7). (a–d) Amplitudes of first to fourth harmonic, respectively, as a function of $x$-location along the channel. (○), measurements by Luth *et al.* [21]; (—), computed, $\Delta x = 0.015$ m, $\Delta t = 0.01$ s; (-----), computed $\Delta x = 0.03$ m, $\Delta t = 0.02$ s; (– – –), computed, $\Delta x = 0.06$ m, $\Delta t = 0.04$ s.

 

primary wave. However, for steeper waves, the stability analysis of Benjamin and Feir has been improved by Crawford *et al.* [26], generally giving lower growth rates at given wave steepness, and having growth rate maxima at perturbation frequencies of $\delta < ka$.

Numerical simulations of the Benjamin–Feir instability are quite demanding, as the computational domain has to cover in the order of $O(100)$ wave periods to allow direct simulation of the recurrence phenomenon, hence requiring high computational efficiency with the present computer technology available. Numerical computations with modulated deep-water wave trains have been performed with potential flow BIEM codes, utilising periodic boundary conditions [4,27] in order to keep the computational domain small, or subdomain division to improve efficiency [6]. In the present work, waves are generated at one end of a long channel with depth $h = 2\pi$ m, with water initially at rest. A primary wave with angular frequency $\omega = 2\pi/T$, $T = 2.006$ s and wave number $k = 1$ m$^{-1}$ is generated with given steepness $ka$ by imposing a second-order Stokes velocity profile. Additionally, two sideband waves with angular frequency $(1 \pm \beta)\omega$, generated by imposing first-order Stokes velocity profiles, are superposed. Throughout the study, the sideband waves have initial amplitudes of $\beta a$, $\beta = 0.05$, and frequency shift $\delta = ka$. The phase shift at $t = 0$ between sideband waves and primary wave is chosen to be $\pi/4$, this being the most unstable case according to Benjamin and Feir.

The simulations are carried out in channels of both 200 and 800 m length, the latter covering about 130 wavelengths. While the horizontal discretisation is chosen to be equidistant, vertically cells are again concentrated towards the free surface ($\alpha = 10$).

In Figure 10(a), the growth of the sideband amplitudes for initial wave steepness $ka = 0.1$ and 0.2 respectively, is compared with the theoretical estimates of Crawford *et al.* [26], showing good agreement. In all simulations, the growth of the upper sideband ($\omega_s = (1 + \delta)\omega$) exceeds that of the lower. Furthermore, particularly with the coarser discretisations, the energy transfer from the carrier wave to the sidebands appears to weaken (see Figure 10(b)) and numerical dissipation is seen to damp the carrier wave.

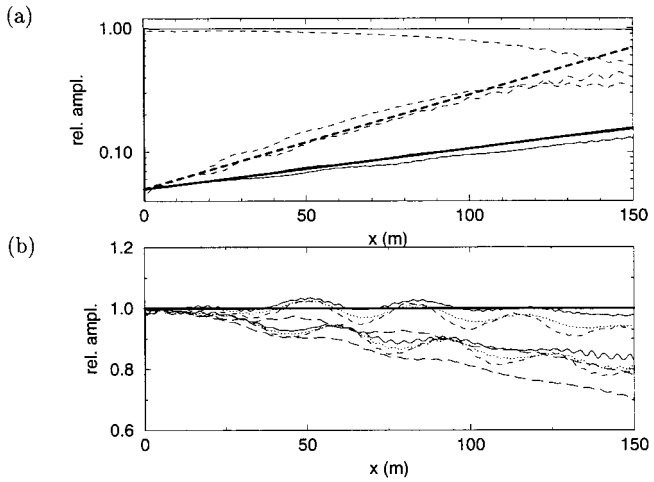


Figure 10. Sideband instability of deep-water wave with period $T = 2.006$ s in a channel of depth $h = 2\pi$ m. (a) Relative amplitude of primary wave upper an lower sideband perturbations, respectively, as function of horizontal position $x$. (—), $ka = \delta = 0.10$. $\Delta x = 0.1$ m, $\Delta t = 0.01$ s; (-----), $ka = \delta = 0.20$. $\Delta x = 0.1$ m, $\Delta t = 0.01$ s; (bold line), side band growth according to Crawford *et al.* [26]. (b) Ratio between computed side band amplitude for $ka = 0.10$ and estimate of Crawford *et al.* as function of $x$. (—), $\Delta x = 0.1$ m, $\Delta t = 0.01$ s; (. . .), $\Delta x = 0.1$ m, $\Delta t = 0.02$ s; (-----), $\Delta x = 0.2$ m, $\Delta t = 0.02$ s; (– – –), $\Delta x = 0.2$ m, $\Delta t = 0.04$ s.

 

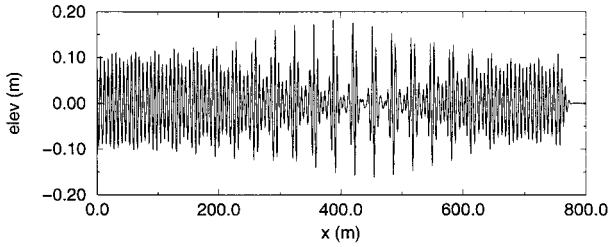


Figure 11. Propagation of deep-water wave ($T = 2.006$ s, $h = 2\pi$ m and $ka = 0.10$) with superposed side band perturbations ($\beta = 0.05$ and $\delta = 0.10$) Elevation profile along channel of 800 m length at $t = 700$ s. Discretisation by $\Delta x = 0.13$ m and $\Delta t = 0.02$ s.

Figure 11 shows the elevation profile as it is computed at time $t = 700$ s for $ka = \delta = 0.10$ along the 800 m long channel. Clearly, at about $x = 400$ m, the wave train is disintegrated into wave pulses, after which the wave evolves back into a near-initial shape about the end of the channel. The estimated recurrence length of about 800 m is larger than the value of 680 m according to the theoretical results of Stiassnie and Kroszynski [28]. Furthermore, the waves approaching the right end of the channel are damped to about 80% of their initial height.

### *4.3. Wave–current interaction*

A steady current is introduced in a channel with a submerged bar (see Figure 12). This is done by adding a steady horizontal component $U_0$ to the imposed velocity boundary condition on the left side boundary and by relaxing the velocity field towards $u_p = U_0$, according to Equation (43), in the wave absorbing region at the right end of the channel. At depth $h_0 = 0.4$ m, the steady velocity component is chosen to be $U_0 = -0.1$ m s$^{-1}$. Due to the small bottom slopes, the steady velocity profile may be assumed to be rectangular. Therefore, simple integral mass and energy balance equations

$$U(h + \eta_m) = U_0 h_0, \qquad \frac{1}{2} U^2 + g\eta_m = \frac{1}{2} U_0^2, \tag{45}$$

can be solved to estimate the steady velocity $U$ and the mean elevation $\eta_m$ as functions of the horizontal position $x$. This yields a velocity of $U_{top} \approx -0.5$ m s$^{-1}$ on top of the bar, which corresponds to a local Froude number of $Fr = U_{top}(g(h + \eta_{top}))^{1/2} \approx -0.47$.

Waves of height $H = 0.005$ m and with periods $T = 2$ and 1 s respectively, are generated to propagate against the mean flow direction. In the case of $T = 2$ s, waves are steepened over the bar with only a minor generation of super-harmonics due to the small amplitude, recovering almost to their initial shape after the bar (see Figure 13). Amplitudes are seen to agree closely

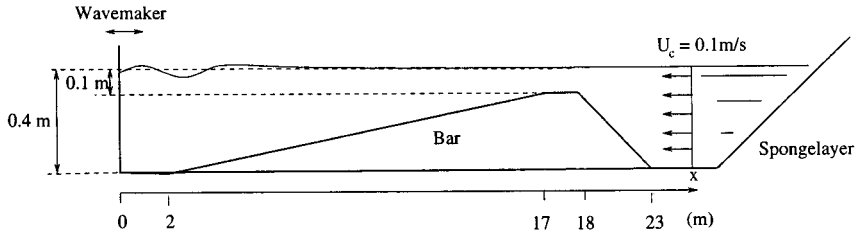


Figure 12. Wave tank with submerged bar on horizontal bottom for studying wave–current interaction.

 

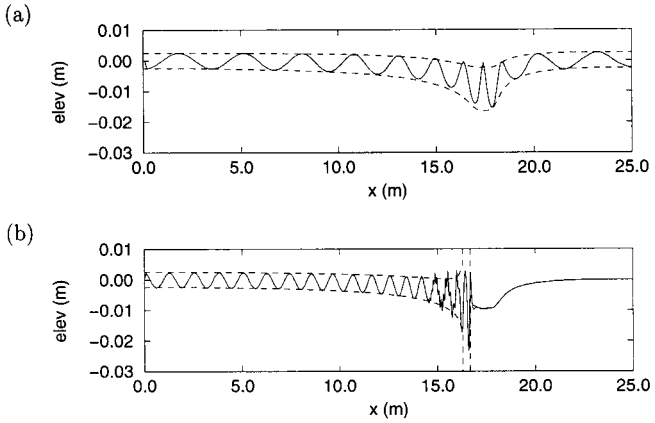


Figure 13. Propagation of waves over a submerged bar with opposing current (see Figure 12). Elevation profiles at $t = 95T$. Initial wave height, $H = 0.005$ m, and current $U_o = 0.1$ m s$^{-1}$ at 0.4 m depth. (a) Wave period $T = 2$ s. (b) Wave period $T = 1$ s. (-----), envelope according to linear wave theory.

with the linear wave theory and the shortened wave length on top of the bar reflects the Doppler shift experienced by the wave. The results are invariant to refinements in discretisation beyond $\Delta x = 0.06$ m and $\Delta t = 0.02$ s. The rather fine time step is necessary due to a

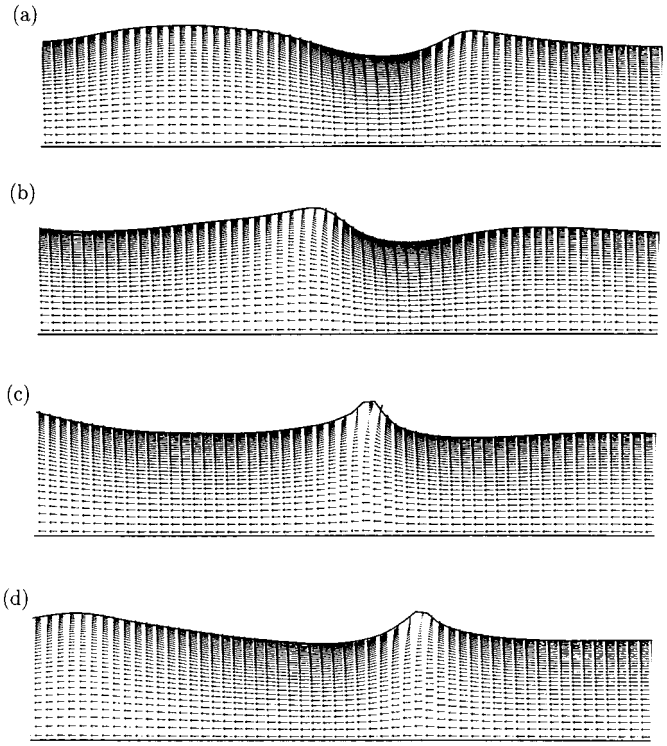


Figure 14. Fluid domain and velocity vectors around blocking point of waves with period $T = 1$ s and initial height $H = 0.005$ m propagating against a steady current (see Figure 12). (a) $t = 95.00T$, (b) $t = 95.25T$, (c) $t = 95.50T$, (d) $t = 95.75T$.

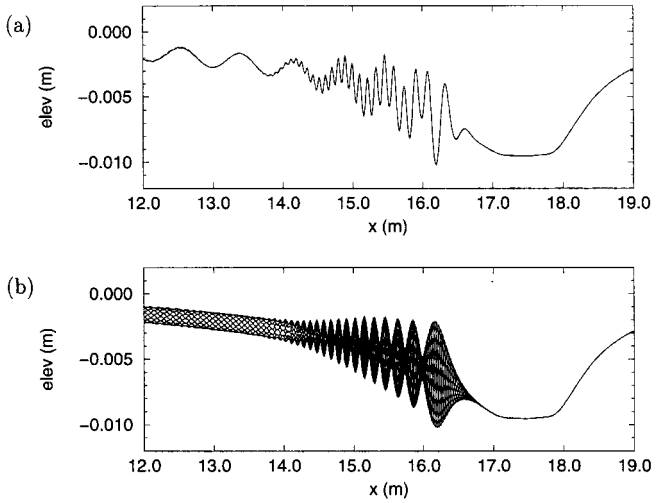


Figure 15. Wave with period $T = 1$ s and initial height $H = 0.001$ m propagating against a steady current (see Figure 12). (a) Elevation profile at $t = 95T$. (b) Elevation profiles at ten phases within a period between $t = 95T$ and $t = 96T$.

CFL-number type stability criterion, becoming more restrictive with the introduction of the steady current.

In the case of $T = 1$ s, waves are blocked on the upward slope because the current velocity exceeds the group velocity of the wave. The blocking point agrees precisely with the location estimated by linear wave theory. In order to resolve the blocking process more closely, the time step is decreased to $\Delta t = 0.005$ s, and in a $2049 \times 33$ grid the horizontal discretisation is locally refined to about $\Delta x \approx 0.01$ m near the blocking point. Waves with initial heights of both $H = 0.001$ and 0.005 m are generated. In Figure 15, the elevation profile shows the incoming wave to be superposed by very short reflected waves, with the wavelength decreasing to $\approx 0.1$ m, as the reflected waves are shortened towards the left and are dissipated rather quickly by numerical damping. In the case of the initial wave height being $h = 0.005$ m, waves of rather large steepness are generated close to the blocking point, and the direction of the local fluid velocity is seen to be reversed in the neighbourhood of the wave crests (see Figure 14).

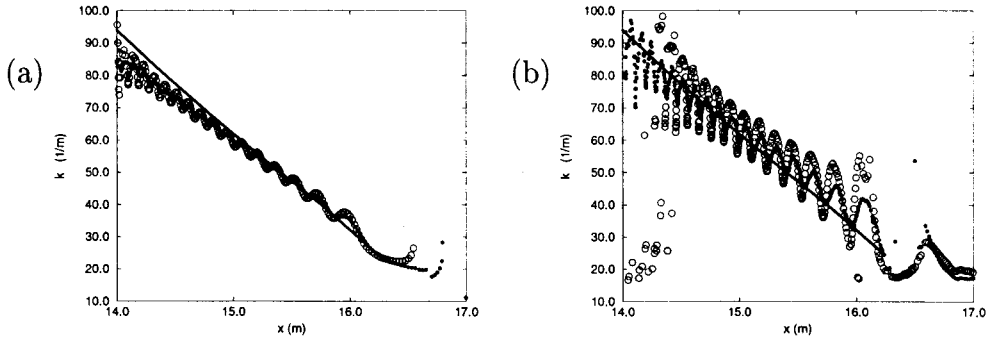


Figure 16. Estimate of wave number of waves being reflected by an opposing current, as a function of the location $x$. (a) initial wave height $H = 0.001$ m; (b) initial wave height $H = 0.005$ m. (○), estimate based on surface elevation; (●), estimate based on vertical surface velocity; (—), theoretical value based on Equations (46) and (47).

 

Assuming the wave train to be fully developed, all variables appear to be periodic with period $T$, seen from a frame of reference being at rest (see also Figure 15). The expression for the constant apparent frequency

$$\sigma = \omega + kU, \qquad \sigma = 2\pi/T, \tag{46}$$

can be solved together with the linear dispersion relation

$$\omega^2 = gk \tanh(k(h + \eta_m)), \tag{47}$$

having two solutions for $k$, the smaller $k_i$ being the wave number of the Doppler shifted incident wave, and the greater $k_r$ being the wave number of the reflected wave, if blocking occurs (see e.g. Reference [29]).

By identifying the wave crests in either the elevation profile, $\eta(x)$ or the vertical component of the fluid velocity $u_y(x)$, the wave number of the reflected wave is estimated as function of $x$ for ten phases within the time interval between $t = 95T$ and $96T$ (see Figure 16). The estimated wave number values are seen to be scattered, but found on average to follow the theoretical estimate quite closely. The scattering increases with increasing initial wave height and it is explained by the Doppler shift which the short reflected waves experience due to the velocity field associated to the longer incident waves.

## 5. DISCUSSION

### 5.1. Accuracy

Error estimates are typically difficult to make for finite volume flow codes due to the many discretisation parameters involved and the non-linearity of the governing equations. Formally, the governing equations are discretised in space to first-order only, the first-order truncation error being due to stretching and skewness of the grid. However, since grids were neither very stretched nor skew in the standing wave test case, convergence rates of second-order are found when varying grid resolution within reasonable limits. In all of the following examples focusing on travelling waves, the horizontal resolution is considered to be of most concern, while the vertical discretisation is chosen to give finer resolution, particularly in connection with deep-water waves.

Both the kinematic boundary condition, Equation (6), and the momentum equation (34), are discretised to second-order in time. Although this second-order convergence rate is seen in the standing wave test for finite time steps, the convergence rate appears to degrade with refinement beyond a certain level. This behaviour is due to the cell-centred variable layout, which requires interpolation of cell-centre values when evaluating fluxes. Hence, in the correction step (37), the predicted velocity $\boldsymbol{u}^*$ is corrected by $\nabla\phi$, where $\phi$ is the solution to Equation (36),

$$\begin{aligned} D(\boldsymbol{G}(\phi)\cdot\boldsymbol{n})^{n+1} &\approx -D(f^*) \approx -D(I((\boldsymbol{u}^n + \Delta t\boldsymbol{R})\cdot\boldsymbol{n}^{n+1})) \\ &\approx -D\left(I\left(\boldsymbol{u}^{*n} + \frac{D(I(\phi^n)\boldsymbol{n}^n)}{v^n}\right)\cdot\boldsymbol{n}^{n+1}\right) - \Delta t D(I(\boldsymbol{R})\cdot\boldsymbol{n}^{n+1}) \\ &\approx D\left(\left(\boldsymbol{G}(\phi^n) - I\left(\frac{D(I(\phi^n)\boldsymbol{n}^n)}{v^n}\right)\right)\cdot\boldsymbol{n}^n\right) - \Delta t D(I(\boldsymbol{R})\cdot\boldsymbol{n}^{n+1}), \end{aligned} \tag{48}$$

and $\boldsymbol{R}$ denotes the discretised RHS of the momentum equation. Since

 

$$D\left(\left(\boldsymbol{G}(\phi^n) - I\left(\frac{D(I(\phi^n)\boldsymbol{n}^n)}{v^n}\right)\right)\cdot\boldsymbol{n}^n\right) = O(\Delta t^0)O(\Delta x^2)O(\Delta y^2), \tag{49}$$

the projection step gives rise to an error, which is decreasing to second-order with the spatial discretisation, but is independent of the temporal discretisation, formally ruining temporal convergence. The error is found to add dissipation to the simulations, fortunately however, it seems to be small compared with other error sources when using time step sizes relevant in practice.

When varying time and space discretisation, numerical stability in the time integration procedure showed to follow a CFL-number type criterion, since both the convective terms and the kinematic boundary condition are treated explicitly. However, no formal stability analysis have been carried out due to the considerable general complexity of the algorithm.

The presented results demonstrate that wave properties and interaction processes are modelled well in both shallow and deep water. In particular, as it is the basis requirement in all the above tests, linear dispersion of gravity waves is described quite well by the method. For numerical resolutions in time and space of $L/\Delta x >= 50$ and $T/\Delta t >= 50$ respectively, the dispersion relation seems to be fulfilled to an accuracy better than 1%. Even amplitude dispersion can be described, as seen in the standing wave test, where non-linearity increases the wave period by 0.2% relative to linear dispersion, although the required accuracy needs a rather fine discretisation.

Since the fully non-linear problem is solved without any assumptions on wave steepness, all kinds of non-linear wave interaction are—at least in theory—included. Triad interactions are successfully simulated both for constant depth and varying depth, and the simulation of the process does not seem to be very sensitive to discretisation. Also, the Benjamin–Feir sideband instability of deep-water waves, being based on quartet wave interactions, is modelled quite well. In general, quartet interactions are significantly weaker than triad interactions and therefore develop more slowly and over longer distances. This makes it a more difficult case to model, as small errors in dispersion may accumulate to significant errors in the wave phase, which again will influence the recurrence length in the phenomenon. Note that the computed recurrence length is significantly longer than the theoretical one.

In the present method, steady or unsteady currents can be introduced directly by specifying proper inflow and outflow boundary conditions, and the description of wave–current interaction is straightforward. In this connection, the successful simulation of wave blocking is believed to be a clear demonstration of the special capabilities of the present code.

### *5.2. Numerical damping*

In contrast to potential flow methods, no energy equation is solved, therefore, the energy balance must emerge from the mass and momentum transport equations. Hence, the main problem for the present method, as for other Euler or Navier–Stokes codes, are errors in the energy conservation. With the above mentioned resolution of $L/\Delta x \approx 50$ and $T/\Delta t \approx 50$, about 0.5% of the energy of the standing wave is dissipated during each period. With $L/\Delta x \approx 50$ and $T/\Delta t \approx 100$, that value is decreased to about 0.1%. The modulated deep-water wave, shown in Figure 11, also discretised by $L/\Delta x \approx 50$ and $T/\Delta t \approx 100$, looses about 0.3% of its energy for every wavelength that the wave is propagating. In this connection, it is important to distinguish between errors in the energy transfer between potential energy and kinetic energy, as it takes place in gravity waves and general numerical dissipation, respectively. The former is mainly determined by the implementation of the pressure boundary condition at the free surface and the choice of time-integration technique employed for the kinematic free-surface

 

condition, and might cause either energy loss or energy gain. The proper treatment of the energy transfer relies heavily on mass conservation, because loss of mass also implies loss of potential energy. Numerical dissipation, on the other hand, is determined by the well-known truncation-error terms in the evaluation of flux terms, particularly the convective terms. Furthermore, the discretisation of the kinematic boundary condition may introduce numerical damping. In particular, numerical damping is associated with the first-order extrapolation procedure of the velocity at free-surface cell faces, Equation (23). This procedure adds dissipation to the system, especially when simulating deep-water waves where the velocity obviously has a non-zero normal gradient at the free surface. However, it has been shown that simple higher-order extrapolation is not numerically stable.

The numerical damping characteristics of the method are not as good as in potential flow methods using equivalent resolution in time and space. However, compared with other free-surface Euler or Navier–Stokes codes, the present code seems to be an improvement in that respect.

### *5.3. Efficiency*

All computations were carried out on a IBM RS/6000 3CT workstation with 128 Mb memory and a 67 MHz Power 2 processor. With this type of computational resource, the method allows accurate simulations of wave trains within $O(50)$ wavelengths over $O(100)$ wave periods.

The memory requirements of the method are not significantly different from common cell-centered finite volume codes on curvilinear grids. While the grid-generation itself at every time step does not cost significant CPU work, as long as algebraic grid generation techniques are employed, two main sources of added CPU work are introduced. First, due to the time-varying grid, recalculation of all geometric coefficients is needed at every time step, where many coefficients could otherwise have been computed once and then stored. Secondly, the introduction of the Poisson equation for the dynamic pressure adds to the computational work, compared with common fractional step methods. Due to the multigrid method employed in the solution of the Poisson equations, the total CPU work per time step increases with problem size as $O(NM)$, $N$ and $M$ being the number of cells in the horizontal and the vertical direction respectively, but it is heavily dependent on the cell aspect ratio and grid stretching. Being a rough estimate, 100 $\mu$s CPU-time is spent by the IBM RS6000 3CT workstation for every cell and time step. These numbers compete well with classical BIEM methods employing direct solution techniques to solve the resulting dense equation systems, at least for large problems because LU-factorisation is an $O(N^3)$ process, $N$ being the number of panels. This comparison will be of a greater advantage to the present method when going to three dimensions. However, iterative solution techniques, being accelerated by multipole expansion techniques, have greatly improved the efficiency of BIEM-methods recently. Furthermore, due to much less numerical damping and the use of higher-order discretisation techniques, space discretisation can be chosen to be coarser than in the present method. Consequently, for wave problems satisfying the assumption of irrotational flow, properly implemented BIEM methods will eventually be most efficient.

Therefore, the objective of the present method is not to compete with potential flow methods for the solution of pure wave problems. The method should be considered as a first step towards a more complete model incorporating the effects of viscous oscillatory flow in combination with free-surface dynamics. Wave–current interaction will be studied in the future, particularly rotational currents. Furthermore, our studies will include both laminar and

 

especially turbulent bottom boundary layers driven by wave motion. Finally, we believe that the present method is a good basis on which models describing the effect of wave breaking, wave driven currents, turbulence, etc. can be developed.

## ACKNOWLEDGMENTS

This work was financed by the Danish National Research Foundation. Their support is greatly appreciated.

## REFERENCES

1. J.M. Floryan and H. Rasmussen, 'Numerical methods for viscous flows with moving boundaries', *Appl. Mech. Rev.*, **42**, 323–41 (1989).
2. W. Tsai and D.K.P. Yue, 'Computations of nonlinear free-surface flows', *Ann. Rev. Fluid. Mech.*, **28**, 249–278 (1996).
3. M.S. Longuet-Higgins and E.D. Cokelet, 'The deformation of steep surface waves on water, I. A numerical method of computation', *Proc. R. Soc. Lond. A*, **350**, 1–26 (1976).
4. J.W. Dold, 'An efficient surface-integral algorithm applied to unsteady gravity waves', *J. Comput. Phys.*, **103**, 90–115 (1992).
5. J. Skourup, M.J. Sterndorff and E.A. Hansen, 'Numerical modelling of wave-structure interaction by a three-dimensional non-linear boundary element method: A step towards the numerical wave tank', *Ocean Eng.*, **19**, 437–460 (1992).
6. P. Wang, Y. Yao and M.P. Tulin, 'Wave group evolution, wave deformation, and breaking: Simulations using Longtank, a numerical wavetank', *Int. J. Offshore Polar Eng.*, **4**, 200–205 (1994).
7. R.K.C. Chan and R.L. Street, 'A computer study on finite-amplitude water waves', *J. Comput. Phys.*, **6**, 68–94 (1970).
8. R.K.C. Chan, 'A generalized arbitrary Lagrangian–Eulerian method for incompressible flows with sharp interfaces', J. *Comput. Phys.*, **17**, 311–331 (1975).
9. C.W. Hirt and B.D. Nichols, 'Volume of fluid (VOF) method for the dynamics of free boundaries', *J. Comput. Phys.*, **39**, 201–225 (1981).
10. B. Ramaswamy, 'Numerical simulation of unsteady viscous free surface flow', *J. Comput. Phys.*, **90**, 396–429 (1990).
11. B. Alesandrini and G. Delhommeau, 'Simulation of three-dimensional unsteady viscous free surface flow around a ship model', *Int. j. numer. methods fluids*, **19**, 321–342 (1994).
12. F.H. Harlow and J.E. Welsh, 'Numerical calculation of time-dependent viscous incompressible flow of fluid with free surface', *Phys. Fluids*, **8**, 2182–2189 (1965).
13. J.F. Thompson, Z.U.A. Warsi and C.W. Mastin, *Numerical Grid Generation*, North-Holland, New York, 1985.
14. M. Rosenfeld, D. Kwak and M. Vinokur, 'A fractional step method for the unsteady incompressible Navier–Stokes equations in generalized coordinate systems', *J. Comput. Phys.*, **94**, 101–137 (1991).
15. Y. Zang, R.L. Street and J.R. Koseff, 'A non-staggered grid, fractional step method for time dependent incompressible Navier–Stokes equations in curvilinear coordinates', *J. Comput. Phys.*, **114**, 18–33 (1994).
16. R.G. Dean and R.A. Dalrymple, *Water Wave Mechanics for Engineers and Scientists*, Prentice-Hall, Englewood Cliffs, NJ, 1984.
17. Y. Agnon and M. Glozman, 'Periodic solutions for a complex Hamiltonian system: new standing water waves', *Wave motion*, **769**, 1–12 (1996).
18. G. Chapalain, R. Cointe and A. Temperville, 'Observed and modelled resonantly interacting progressive water-waves', *Coastal Eng.*, **16**, 267–300 (1992).
19. P.A. Madsen and O.R. Sørensen, 'Bound waves and triad interactions in shallow water', *Ocean Eng.*, **20**, 359–388 (1993).
20. S. Beji and J.A. Battjes, 'Experimental investigation of wave propagation over a bar', *Coastal Eng.*, **19**, 151–162 (1993).
21. H.R. Luth, G. Klopman and N. Kitou, 'Projects 13G: Kinematics of waves breaking partially on an offshore bar; LDV measurements for waves with and without a net onshore current', *Technical Report H1573*, Delft Hydraulics, 1994.
22. S. Beji and J.A. Battjes, 'Numerical simulation of nonlinear wave propagation over a bar', *Coastal Eng.*, **23**, 1–16 (1994).
23. T. Ohyama, W. Kioka and A. Tada, 'Applicability of numerical models to nonlinear dispersive waves', *Coastal Eng.*, **24**, 297–313 (1995).
24. P.A. Madsen, B. Banijamali, H.A. Schäffer and O.R. Sørensen, 'Boussinesq type equations with high accuracy in dispersion and nonlinearity', in *ICCE 96, 25th Coastal Engineering Conference*, Orlando, Florida, 1996.

 

25. T.B. Benjamin and J.E. Feir, 'The disintegration of wave trains on deep water, part 1', *J. Fluid Mech.*, **27**, 417–430 (1967).
26. D.R. Crawford, B.M. Lake, P.G. Saffman, and H.C. Yuen, 'Stability of weakly nonlinear deep-water waves in two and three dimensions', *J. Fluid Mech.*, **105**, 177–191 (1981).
27. J. Skourup, 'Evolution and kinematics of a modulated wave train by use of the boundary element method', *International symposium: Waves—physical and numerical modelling*, Vancouver, 1994.
28. M. Stiassnie and U.I. Kroszynski, 'Long-term evolution of unstable water wave train', *J. Fluid. Mech.*, **116**, 207–225 (1982).
29. D.H. Peregrine, 'Interaction of water waves and current', *Adv. Appl. Mech.*, **16**, 10–117 (1976).

 